Modeling of Heat Transfer and Fluid Flow in the Laser Multilayered Cladding Process

FANRONG KONG and RADOVAN KOVACEVIC

The current work examines the heat-and-mass transfer process in the laser multilayered cladding of H13 tool steel powder by numerical modeling and experimental validation. A multiphase transient model is developed to investigate the evolution of the temperature field and flow velocity of the liquid phase in the molten pool. The solid region of the substrate and solidified clad, the liquid region of the melted clad material, and the gas region of the surrounding air are included. In this model, a level-set method is used to track the free surface motion of the molten pool with the powder material feeding and scanning of the laser beam. An enthalpy–porosity approach is applied to deal with the solidification and melting that occurs in the cladding process. Moreover, the laser heat input and heat losses from the forced convection and heat radiation that occurs on the top surface of the deposited layer are incorporated into the source term of the governing equations. The effects of the laser power, scanning speed, and powder-feed rate on the dilution and height of the multilayered clad are investigated based on the numerical model and experimental measurements. The results show that an increase of the laser power and powder feed rate, or a reduction of the scanning speed, can increase the clad height and directly influence the remelted depth of each layer of deposition. The numerical results have a qualitative agreement with the experimental measurements.

DOI: 10.1007/s11663-010-9412-2
© The Minerals, Metals & Materials Society and ASM International 2010

I. INTRODUCTION

LASER cladding is used widely to create various surface coatings with a significant thickness that effectively can protect substrates from harsh service conditions,[1–4] However, the correct selection of the process parameters for the building or printing of spatial structures of the required geometry is a difficult task. The processing parameters such as the laser beam power, beam intensity in the processing zone, scanning speed, and powder feed rate have a strong relationship with each other through mutual interaction, and they have a distinct influence on the mechanical properties of the remelted materials and cladding qualities.[4–6] In laser cladding, considering that the severe temperature gradient and mass transportation in the molten pool are caused by the convection of the liquid phase, the geometry of the molten pool absolutely plays a vital role in finally deciding the clad quality. For example, a too-small molten pool resulting from insufficient absorption of laser energy may result in a lack of melting and thus, an insufficient bond of consecutive layers. Conversely, an overlarge penetration will damage the cladding quality because of the diffusion of substrate material into the clad layer,[7] which makes the quality of the surface clad defective. In addition, many intermediate physical phenomena in the laser cladding process are extremely difficult to observe experimentally because of the presence of intense laser irradiation. Therefore, modeling combined with an experimental validation is an effective way to reveal the complete physical phenomena in the laser cladding process.

So far, most efforts of thermal modeling in laser cladding have concentrated on the conduction mode of heat transfer.[8–10] Strong sources of heat convection definitely are in the molten pool as a result of temperature-dependent surface tension variation over the molten pool free surface and a density variation in the bulk of the molten pool, respectively. However, a limited attempt has been accomplished to study the fluid flow combined with solute diffusion in the molten pool of laser cladding. In the early work of the modeling of laser cladding, Kar and Mazumder[11] developed a one-dimensional conduction model to determine the composition of the alloys and cooling process. Hoadley and Rappaz[12] presented a two-dimensional (2D) model to calculate the temperature in the steady-state condition during laser cladding. Later, Han *et al.*[13] solved 2D fluid flow and energy equations to predict the temperature distribution and geometry of the molten pool in the laser cladding process. Recently, Toyserkani *et al.*[14] presented a three-dimensional (3D) transient finite-element model for laser cladding with a powder injection. They decoupled the interaction between the molten pool and the powder to simplify the thermal analysis and the molten pool boundary condition calculation. In addition, many studies have been performed that include convection in the laser melting and

FANRONG KONG, Research Engineer, and RADOVAN KOVACEVIC, Herman Brown Chair Professor, are with the Center for Laser-aided Manufacturing, Southern Methodist University, Dallas, TX 75205. Contact e-mail: kovacevi@lyle.smu.edu
Manuscript submitted July 10, 2009.
Article published online July 30, 2010.

laser alloying processes but presume the free surface of the molten pool to be flat with no material addition.[15,16] Moreover, most published solutions are limited to a simplified case with a presumed clad geometry.[17,18] The 3D numerical model presented by He and colleagues[19,20] to study the temperature and fluid flow in the molten pool during the laser cladding of H13 steel powder used a level-set approach to track the free surface evolution of the molten pool. Their work focused on single layered cladding for the single-track[19] and double-track[20] cases. For laser multilayered cladding, including the laser remelting of subsequent layers, the model becomes considerably complex. For subsequent layers, the growing distance from the base hinders the heat conduction and promotes the convection and radiation mechanisms.[21]

The simulation of the fluid flow of the molten pool, temperature distribution, and thermal stress field have been implemented mainly with high-power beam material processing methods and are based on assumptions that ignore some important physical phenomena. Considering laser cladding along with the molten pool, a complicated interaction exists among the laser, substrate material, and powder material. It is necessary to offer a much more reliable numerical model to describe better the related complicated physics, especially the heat transfer and fluid flow in the molten pool area during the laser multilayered cladding process.

The purpose of this work is to develop a solid–liquid–gas-unified model of predicting the flow velocity of the liquid phase and temperature distribution during the laser multilayered cladding (LMC) process in which the solid region of the substrate and solidified clad, the liquid region of the molten pool existing in the clad, and the gas region of the surrounding air are included.[21] An enthalpy–porosity model is applied to deal with the solidification and melting of the deposited layer, and a level-set method is used to track the evolution of the free surface of the molten pool with the powder feeding and scanning of the laser beam. Moreover, the complicated physical phenomena occurring at the liquid–gas (L/G) interface, including the laser heat input and heat losses from forced convection and heat radiation, are incorporated into the governing equations by source terms. In addition, considering that a uniform fixed mesh took considerable time to run the program that was applied in He and colleagues' model,[19,20] a nonuniform adaptive mesh will be used in our discrete model. The adaptive mesh will reduce the computational cost and reasonably improve the convergence efficiency to make it available for running in a personal computer. Considering that H13 tool steel with a high wear resistance has been used widely as a clad material to improve the surface performance of carbon steel in machine parts, in this study, H13 steel powder is deposited onto AISI 4140 steel substrate, and the obtained experimental results are used to validate the developed model. The effects of the laser power input, laser beam-scanning speed, and powder feed rate on the geometry of the clad bead, temperature distribution, and fluid flow in the molten pool are investigated in detail.

II. MATHEMATICAL MODELING

Figure 1(a) shows the experimental setup of laser cladding with powder injection, and Figure 1(b) describes the relevant schematic view of the LMC process. The computational domain initially consists of the substrate (solid phase) and the air above the substrate (gas phase). The powders of the controlled flow rate are delivered onto the substrate concentrically with the laser beam. A small area of the surface of the substrate or the previously deposited layer is irradiated by the laser beam to form the molten pool. A build-up with a designed shape and composition is formed with the multilayered scanning of the laser head and is controlled by a computer numerical control (CNC) positioning system with continuous metal powder feeding. Considering that the microstructural and macrostructural interaction mechanism among the laser beam, powder flow, and substrate is complicated, many influencing factors exist between the mass and heat transfer of the molten pool and between the deposited layer and substrate. To establish the mathematical model describing the whole deposition process, some fundamental assumptions are taken into consideration as follows: (1) the laser power intensity and powder flow distribution obey the

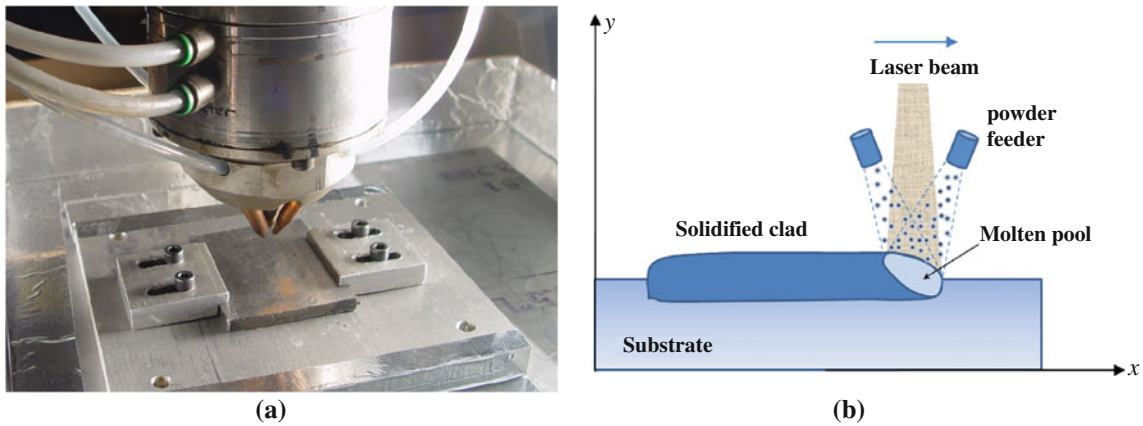

Fig. 1—(*a*) Experimental setup and (*b*) schematic view of the laser-based multilayered cladding process.

Gaussian distribution, respectively; (2) the liquid flow is incompressible and has a laminar flow, and the gas flow is incompressible; (3) the mixture region of the solid phase and liquid phase is considered to be the mushy zone[9]; and (4) the effect of the shielding gas pressure on the surface profile and fluid flow in the molten pool is ignored.

A. *Tracking of the Free Surface of the Molten Pool, the L/G Interface*

In the LMC process, the flow in the molten pool is driven mainly by surface tension, thermocapillary force, and impaction of the recoiling pressure of the metal vapor on the molten pool surface.[9] To track the evolution of the molten pool surface, a level-set approach[19,20,22,23] is introduced to deal with the complex physical phenomenon occurring on the free surface of the molten pool, as shown in Figure 2. It is a satisfying way of viewing the well-known kinematic boundary condition of the interface. The equation, which has been thought to be valid for the interface only, can be defined for the entire space that contains the interface by considering it as one level set of a well-created function ϕ.

The interface shape function ϕ is defined all over the domain, but for a specific level set, the value of the function is the constant B, which is expressed as follows:

$$\phi = \phi(x, y, t) = \mathrm{B} \qquad [1]$$

For example, B is zero for the zero level set ϕ_0. Given the material derivative of a constant is zero, we have the following:

$$\frac{D\phi}{Dt} = 0 = \frac{\partial \phi}{\partial t} + \vec{u}\cdot\nabla\phi \qquad [2]$$

Here, we know that $\nabla\phi/|\nabla\phi|$is the surface normal $\vec{n}$ on the given level set; thus, the earlier equation becomes the following:

$$\frac{\partial \phi}{\partial t} + \vec{u}\cdot\vec{n}|\nabla\phi| = 0 \qquad [3]$$

Here, $\vec{u}\cdot\vec{n}$ is the speed of the interface in the normal direction, which usually is named the speed function or force function and written as F_{LV}. Thus, we have the following:

$$\varphi_t + F_{\mathrm{LV}}|\nabla\varphi| = 0 \qquad [4]$$

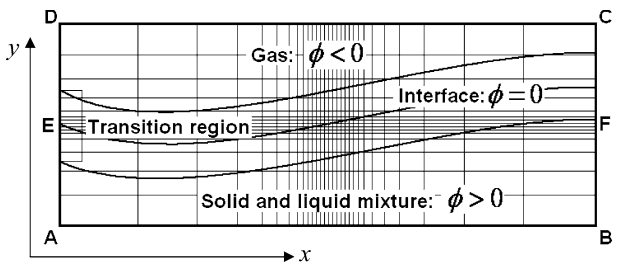

Fig. 2—Schematic of level-set approach with adaptive mesh.

Equation [4] is valid not only for the zero level set ϕ_0 but also for all other level sets because the equation holds good for any values of B. Equation [4] is the starting point of the level-set method. It is apparent that the equation is a partial differential equation of the hyperbolic type and is changed to capture the interface in the one-order-higher dimensional space by solving the equation.[23] According to the physics of the LMC process, F_{LV} can be divided into the following parts:

$$F_{\mathrm{LV}} = F_{\mathrm{e}} + F_{\mathrm{curv}} + F_{\mathrm{adv}} \qquad [5]$$

where $F_{\mathrm{curv}} = -\in\kappa$ is a velocity function dependent on the curvature of the L/G interface. $F_{\mathrm{adv}} = U(x, y, t) \times \vec{n}$ is a convection velocity function. F_{e} is a velocity function that is dependent on the motion of the L/G interface based on the powder deposition. To simplify the modeling procedure, it is assumed that the powder-feeding process is consecutive and steady, and the powder is fully melted when reaching the molten pool surface during the LMC process. Under these conditions, F_{e} can be expressed as follows:

$$F_e = \begin{cases} \frac{2\eta'\dot{m}}{\pi R'^2}\exp\left(-\frac{2r'^2}{R'^2}\right)\Big/(\rho_l V_s) & r' \le R' \\ 0 & r' > R' \end{cases} \qquad [6]$$

where r' is the distance from the center of the top surface of the molten pool and R' is the effective radius of the powder's feeding flow; $\dot{m}$ is the mass of the powder feeding in the unit interval; η' is an efficient utilization ratio of powder; ρ_l is the density of the powder in the liquid phase; and V_s is the scanning speed.

To simplify the level-set function, the term for the surface tension is ignored. However, the impact of surface tension on the convection of the molten pool is taken into account in the Navier–Stokes function by the level-set function ϕ. Hence, the level-set function can be updated as follows:

$$\phi_t + F_{\mathrm{e}}|\nabla\phi| + U(x, y, t)\cdot\nabla\phi = 0 \qquad [7]$$

To extend the zero level set to the entire domain, the level-set function should be well defined and the signed distance is chosen as follows:

$$\phi(\vec{x}, t = 0) = \pm d \qquad [8]$$

where, d denotes a distance from a point $\vec{x}$ to the L/G interface. The point exists in the gas region when $\phi(x, t) < 0$, the point exists in the mixture of solid and liquid region when $\phi(x, t) > 0$, and the point exists at the L/G interface when $\phi(x, t) = 0$.

According to the inherent characteristics of the level-set approach, the reinitialization of the level-set function should be implemented at each time step, which could update the level-set function ϕ to reobtain the zero-value position of the level-set function (*i.e.*, the free surface of the deposited layer).

To overcome the numerical difficulties at the interface caused by the properties change, such as the density and viscosity, it is assumed that the L/G interface has a fixed transition thickness, and that the

physical properties change smoothly along the thickness of the transition zone. The modified Heaviside function[8] employed to smooth the properties change is expressed as follows:

$$H_\varepsilon(\phi) = \begin{cases} 0 & \text{if} \quad \phi < -\varepsilon \\ 0.5\left[1 + \frac{\phi}{\varepsilon} + \frac{1}{\pi}\sin\left(\frac{\pi\phi}{\varepsilon}\right)\right] & \text{if} \quad |\phi| \le \varepsilon \\ 1 & \text{if} \quad \phi > \varepsilon \end{cases} \quad [9]$$

where ε is half of the transition zone thickness. Thus, the density and viscosity in the whole calculation region, including the surrounding air, molten pool zone, solidified deposited layer, and substrate, can be modified as follows:

$$\rho = \rho_{\text{sl}} H_\varepsilon(\phi) + [1 - H_\varepsilon(\phi)]\rho_{\text{g}} \quad [10]$$

$$\mu = \mu_{\text{sl}} H_\varepsilon(\phi) + [1 - H_\varepsilon(\phi)]\mu_{\text{g}} \quad [11]$$

where ρ_{sl} denotes the density of the mixture region for the solid and liquid phases, ρ_{g} denotes the density of air, μ_{sl} denotes the viscosity of the mixture region for the solid and liquid phases, and μ_{g} denotes the viscosity of air. Other physical properties in the unified model also are complemented accordingly following Eqs. [10] and [11].

The Delta function $\delta(\phi)$ deriving from the Heaviside function is applied to ensure the force acting on the L/G interface is as follows:

$$F_{\text{n}} = (p_v + \tau\kappa)\delta(\phi) \quad [12]$$

$$F_{\text{t}} = -\frac{d\tau}{dT}\nabla_s T\delta(\phi) \quad [13]$$

where τ is the surface tension coefficient, κ is the curvature, p_v is the shield gas pressure, and ∇_s is the surface nabla. F_{n} andF_{t} refer to the tangent and normal components of interface force, respectively. The Delta function may be expressed as follows:

$$\delta(\varphi) \equiv \begin{cases} \cos(\pi|\varphi|/(2\varepsilon)) & \text{if} \quad |\varphi| \le \varepsilon, \\ 0 & \text{otherwise} \end{cases} \quad [14]$$

According to the level-set function ϕ, the surface normal and tangent vector of the molten pool may be shown as follows:

$$n = \frac{\nabla\phi}{|\nabla\phi|}\Big|_{\phi=0} \quad [15]$$

$$\kappa = \nabla \times \left(\frac{\nabla\phi}{|\nabla\phi|}\right)\Bigg|_{\phi=0} \quad [16]$$

B. *Governing Equations*

The calculation domain illustrated in Figure 2 includes the substrate and deposited layer (solid phase), the molten pool (liquid phase), and part of the gas region (gas phase). The continuum model, which introduces the Darcian damping term, governs the conservations of mass, momentum, and energy for the mushy region, liquid region, and solid region. This model also governs the conservation of the solute diffusion of the solid and liquid region by the "mixture of material property" method.[9] This method applies the average physical parameters that consider the mass or volume ratio of the solid and liquid phases in a certain cell to represent the difference of the thermal physical property of the material in the solid and liquid regions. The continuum model may be described as follows:

Mass conservation equation:

$$\frac{\partial\rho}{\partial t} + \nabla\cdot(\rho\vec{V}) = 0 \quad [17]$$

Solute diffusion equation:

$$\frac{\partial}{\partial t}(\rho C_i) + \nabla\cdot(\rho\vec{V}C_i) = \nabla(\dot{\rho} f_l D\nabla C_i) \quad [18]$$

Momentum conservation equations:

$$\frac{\partial(\rho u)}{\partial t} + \frac{\partial(\rho uu)}{\partial x} + \frac{\partial(\rho vu)}{\partial y} = \mu\left(\frac{\partial^2 u}{\partial x^2} + \frac{\partial^2 u}{\partial y^2}\right) - \frac{\partial p}{\partial x} + S_x \quad [19]$$

$$\frac{\partial(\rho v)}{\partial t} + \frac{\partial(\rho uv)}{\partial x} + \frac{\partial(\rho vv)}{\partial y} = \mu\left(\frac{\partial^2 v}{\partial x^2} + \frac{\partial^2 v}{\partial y^2}\right) - \frac{\partial p}{\partial y} + S_y \quad [20]$$

where the source terms are expressed as follows:

$$S_x = -\frac{\mu}{E}(u - V_s) + \vec{e}_x\cdot\left(-\tau\kappa(\phi)\nabla\phi + \nabla_s T\frac{d\tau}{dT} - p_v\right)\delta(\phi) \quad [21]$$

$$S_y = -\frac{\mu}{E}v + \vec{e}_y\cdot\left(-\tau\kappa(\phi)\nabla\phi + \nabla_s T\frac{d\tau}{dT} - p_v\right)\delta(\phi) + \rho g\beta(T - T_{\text{m}}) \quad [22]$$

And the energy conservation equation is written as follows:

$$\rho\frac{\partial h}{\partial t} + \rho\left(\frac{\partial h}{\partial x}u + \frac{\partial h}{\partial y}v\right) = k\left(\frac{\partial^2 T}{\partial x^2} + \frac{\partial^2 T}{\partial y^2}\right) + S_{\text{E}} \quad [23]$$

In the aforementioned equations, ρ is the mean density, $\vec{V}$ is the velocity vector, and u and v are the components of $\vec{V}$ along the x and y coordinates, respectively. C_i is the mass fraction of solute i, D is the solute diffusion coefficient, p is the pressure, μ is the dynamical viscidity of the liquid phase, p_v is the recoil vapor pressure,[14] and $\vec{e}_x$ and $\vec{e}_y$ are the unit vectors along the x and y coordinates, respectively. T_{m} is the melting point of material, β is the buoyancy coefficient, E is the permeability of the two-phase mushy zone, h is the enthalpy, T is the temperature, k is the heat conductivity, V_{s} is the scanning speed, and S_{E} is the source term of the energy equation including the

laser heat input and heat losses caused by convection and radiation occurring at the L/G interface as follows:

$$S_E = [q''_{\text{laser}} - \sigma \Im (T^4 - T_\infty^4) - h_c(T - T_\infty)]/(2\varepsilon)\cdot\delta(\phi) \quad [24]$$

where, σ is the Stefan–Boltzmann constant, $\Im$ is the radiation emissivity, T_∞ is the ambient temperature, and h_c is the convection coefficient. q''_{laser} is the laser energy at the L/G interface that obeys the following Gaussian distribution:

$$q''_{\text{laser}} = \frac{2\eta P_{\text{laser}}}{\pi R_l^2}\exp\left(-\frac{2r^2}{R_l^2}\right) \quad [25]$$

where, P_{laser} is the laser power, R_l is the effective beam spot radius, r is the distance from the calculation cell to the beam center, and η is the absorptivity coefficient.

Because the solid phase and liquid phase exist simultaneously as one cell in the mushy region, a mixture of properties are used for the density, specific heat, conductivity, enthalpy, and velocity vector, and are defined as follows:

$$\rho_{\text{sl}} = g_{\text{s}}\rho_{\text{s}} + g_{\text{l}}\rho_{\text{l}} \quad [26]$$

$$c_{\text{sl}} = f_{\text{s}}c_{\text{s}} + f_{\text{l}}c_{\text{l}} \quad [27]$$

$$k_{\text{sl}} = g_{\text{s}}k_{\text{s}} + g_{\text{l}}k_{\text{l}} \quad [28]$$

$$h_{\text{sl}} = f_{\text{s}}h_{\text{s}} + f_{\text{l}}h_{\text{l}} \quad [29]$$

$$V_{\text{sl}} = f_{\text{s}}V_{\text{s}} + f_{\text{l}}V_{\text{l}} \quad [30]$$

where, f_{s} and f_{l} refer to mass fractions of the solid and liquid phases, and g_{s} and g_l are the volume fractions of the solid and liquid phases. When the corresponding volume fractions approach the value of zero or one, the mixture properties reflect the presence of the molten pool or solid region. The phase enthalpy for solid and liquid can be described as follows:

$$h_{\text{s}} = \int_0^T c_{\text{s}}dT = c_{\text{s}}T \quad [31]$$

$$h_l = \int_0^{T_s} c_{\text{s}}dT + L_{\text{m}} + \int_{T_s}^{T} c_l dT = c_l T + (c_{\text{s}} - c_l)T_{\text{s}} + L_{\text{m}} \quad [32]$$

where L_{m} is the latent heat of melting, and T_{s} and T_{l} are the solidus and liquidus temperatures, respectively.

In the Eqs. [21] and [22], the first set of terms on the right-hand sides are the Darcian damping terms, and E is the permeability of the two-phase mushy zone, which is modeled as a porous media. Following the method presented by Bennon and Incropera,[24,25] the current study employs the following Kozeny–Carman equation for permeability:

$$E = \frac{E_0 g_{\text{l}}^3}{(1 - g_{\text{l}})^2} \quad [33]$$

where, E_0 is the permeability coefficient dependent on the material microstructure. The calculation of the permeability coefficient E_0 requires the knowledge of the growth morphology specific to the alloy[25]. The value of E in the damping term approaches infinity while in the liquid region, whereas, the value of E approaches zero while in the solid region.

C. *Boundary Conditions*

As mentioned previously, the physical phenomena occurring at the S/L interface and in the L/G interface are implemented implicitly as part of the source terms of the energy and momentum conservation equations, correspondingly. In the present study, it is assumed that the gas phase boundaries DC, DE, and CF are thermally insulated boundaries; however, there convection and radiation heat transfer exists among the solid phase boundaries AB, AE, BF, and ambient that also are shown in Figure 2.

D. *Numerical Procedure*

Much of the published literature has paid attention to predicting numerically the transient heat transfer and fluid flow phenomena in laser-based material processing. However, considering that the fixed mesh is used in those numerical works,[19] a large amount of grids are needed throughout the whole model to keep enough of the mesh density at the deposited layers where the moving molten pool passes through to acquire enough computational accuracy. Therefore, the expensive computational cost limits the further expansion of the numerical modeling to include multilayer or multitrack deposition. To improve further the calculation efficiency of the numerical modeling, a self-adaptive asymmetric grid is applied in this work (Figure 2). Finer nodes are distributed near and inside the molten pool in order to acquire the precise simulation. Much sparser nodes are distributed far from the molten pool so as to reduce the whole calculation cost.

In this study, the numerical implementation of the transport equations is based on the Semi-Implicit Method for Pressure-Linked Equation-Consistent (SIMPLEC) algorithm with staggered grids, initially presented by Patankar.[26] The detailed procedure can be depicted in Figure 3. A computationally cost-effective procedure known as the line by line was developed to solve the discretization equations for a group of points along the same row or column. This method of solving a group of nodes all at the same time is, in essence, a combination of the tridiagonal matrix algorithm and the Gauss–Seidel method.[26] At the same time, the level-set equation is solved to track the evolution of the L/G interface that is coupled with the solution of the momentum and energy equations. The detailed

procedure can be depicted through the following iterative steps[19,22,26]:

(a) Initialize the calculation node variables: let the level-set function ϕ be the signed normal distance to the surface. Set u and v as the divergence-free velocity, identically zero in the whole calculation domain; T as room temperature; and p as the relative reference pressure.

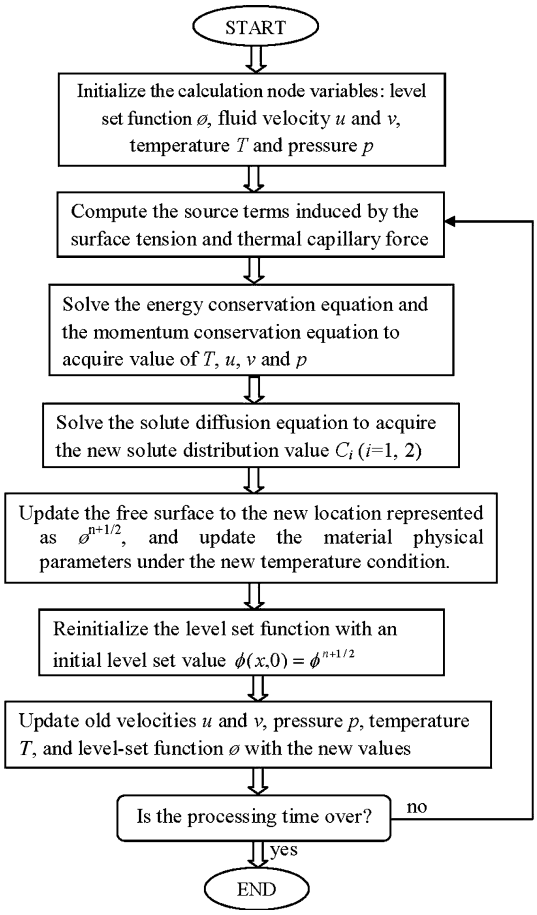

Fig. 3—Flowchart of numerical procedure in the solid–liquid–gas unified modeling.

(b) Compute the source terms induced by the surface tension and thermal capillary force in which the effects of the shielding gas pressure and recoil vapor pressure are neglected to track the evolution of the surface profile of the deposited layer.

(c) Use the SIMPLEC algorithm[26] with staggered grids to solve the energy conservation equation and use the momentum conservation equation to acquire the new temperature distribution, velocity, and pressure values.

(d) Based on the convergence values of the temperature and fluid velocity in step (c), solve the solute diffusion equation to acquire the new solute distribution value.

(e) Advance the level-set function in time using a second-order space convex scheme,[26] and update the free surface to the new location represented as $\phi^{n+1/2}$. Update the material physical parameters under the new temperature condition.

(f) Reinitialize the level-set function by solving the following equation to be steady state with an initial level set value $\phi(x, 0) = \phi^{n+1/2}$:

$$\phi_\tau = S_\alpha(\phi^{n+1/2})(1 - |\nabla\phi|) \qquad [34]$$

where τ is the artificial time, $S_\alpha(*)$ is the function that gives the sign of the argument *, and α is the smoothing factor.

(g) Update the old velocities, the pressure, the temperature, and the level-set function with the new values, and go back to step (b) for the next iteration until the end of the simulation time is reached.

III. EXPERIMENTAL VALIDATION AND CASE ANALYSIS

An AISI 4140 steel plate is used as a substrate, and the H13 tool steel powder is used as a coating material.

Table I. Main Physical Parameters

Property	Value of H13 Steel	Value of AISI 4140 Steel
Ambient temperature, T_∞ (K) (°C)	298 (25 °C)	298 (25 °C)
Solid viscosity, μ_s (kg × m^{-1} s^{-1})	7800	8000
Dynamic viscosity, μ_l (kg × m^{-1} s^{-1})	6.0 × 10^{-3}	5.0 × 10^{-3}
Solid specific heat, C_s (J × kg^{-1} K^{-1})	440	461
Liquid specific heat, C_l (J × kg^{-1} K^{-1})	440	461
Solid thermal conductivity, k_s (W × m^{-1} K^{-1})	42.4	11.21 + 0.017*T
Liquid thermal conductivity, k_l (W × m^{-1} K^{-1})	42.4	33.31
Solid density, ρ_s (kg × m^{-3})	7900	8360
Liquid density, ρ_l (kg × m^{-3})	7900	8360
Latent heat of fusion, L_m (J × kg^{-1})	3.3 × 10^5	2.1 × 10^5
Solidus temperature, T_s (K) (°C)	1623 (1350 °C)	1573 (1300 °C)
Liquidus temperature, T_l (K) (°C)	1673 (1400 °C)	1628 (1355 °C)
Radiation emissivity, ∋	0.1	0.1
Surface tension coefficient, τ (kg × s^{-2})	0.836 (at 933 K (660 °C))	0.860 (at 933 K (660 °C))
Surface tension coefficient with temperature, $\partial\tau/\partial$T (kg × s^{-2} K^{-1})	–0.43 × 10^{-3}	–0.35 × 10^{-3}
Stefan–Boltzmann's constant, σ (W × m^{-2} K^{-4})	5.67 × 10^{-8}	5.67 × 10^{-8}

The original size of the H13 tool steel powder is 50 to 100 μm. The compositions of the AISI 4140 and H13 steels are referenced from the Reference 3. The physical parameters of the H13 tool steel and 4140 steel are listed in Table I. An Nd:YAG laser with a maximum power of 1 kW in a continuous wave form is used to produce the coatings. Laser power is 150 W, 225 W, and 300 W, respectively. An absorptivity of laser power is set at 30 pct according to the previous publication,[9] which also is validated by the comparison between the numerical simulation and the validation experiments in this study. The effective diameter of the focal point of the laser beam used in the modeling is 0.8 mm. In this case, the laser beam scanning speeds are 8, 10, and 12 mm/s, respectively. A powder feed system is used for the direct injection of powders into the molten pool with argon flow as a powder carrier. The H13 tool steel powder is injected into the molten pool by the powder feeders through four nozzles, each of which are 1 mm in diameter. The effective diameter of the powder flow stream used in the modeling is 1 mm. The effective powder feed rates used in the modeling are 0.01, 0.02, and 0.03 g/s, respectively, and are verified experimentally. The three-layer beads are deposited at various scanning speeds, laser powers, and powder feed rates.

The dimensions of the substrate are 25 mm × 5 mm (length × height); the dimensions of the simulation region are 25 mm × 10 mm. The experimental setup of the deposited multilayer during the laser-based powder deposition process is shown in Figure 1(a). The clad, with a length of 20 mm, is distributed symmetrically at the substrate. In this study, the three-layer laser deposition manufacturing process is simulated such that the surface tension gradient and the buoyancy dependent on the temperature gradient are considered the driving forces of flow field in the molten pool. The transverse cross sections of the deposited beads are cut for metallographic studies, and optical microscopy is used for microstructure inspection of the etched coupons.

IV. RESULTS AND DISCUSSION

The transient temperature field of the laser-based multilayered cladding process is shown in Figure 4.

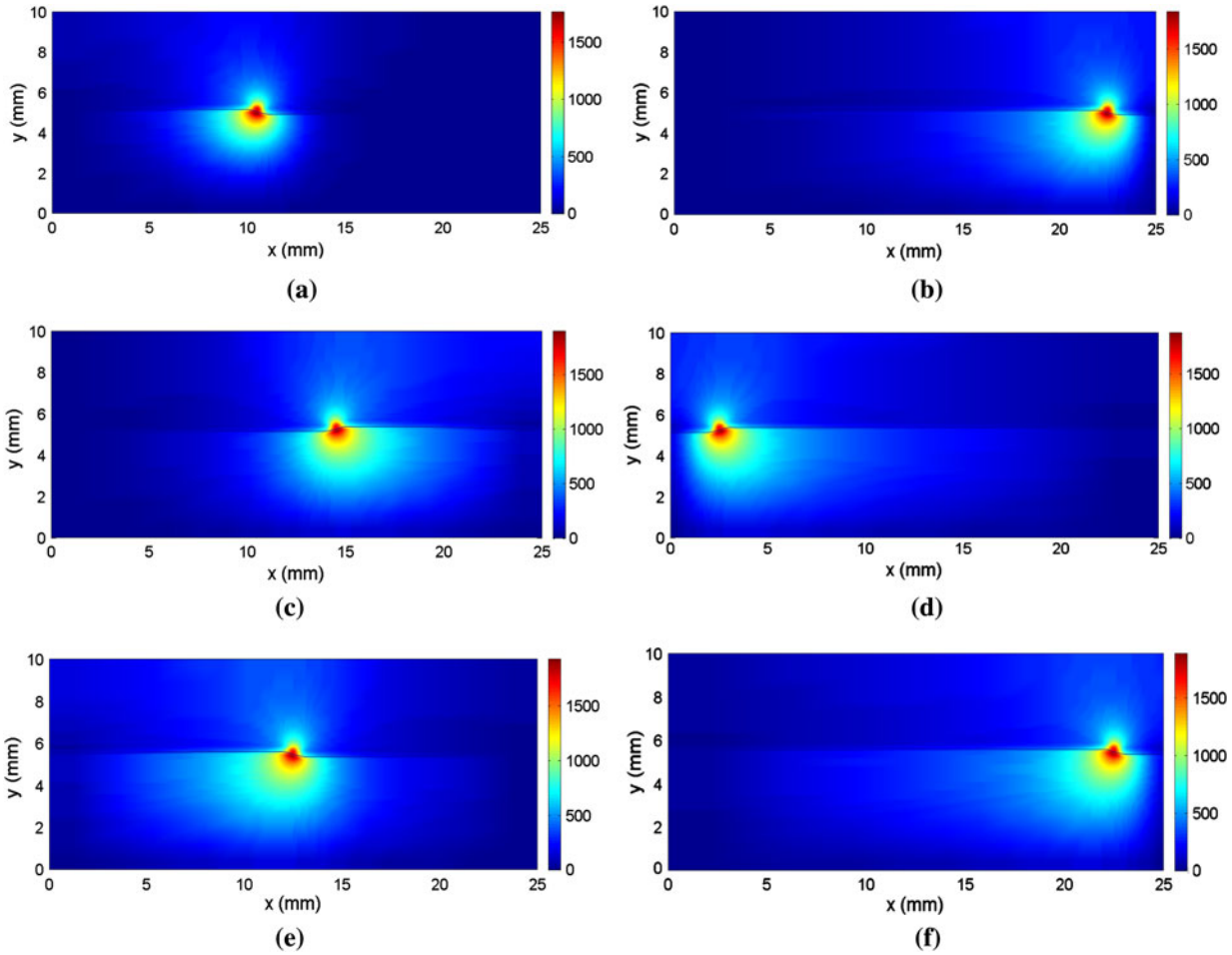

Fig. 4—Transient temperature distributions in the laser multilayer cladding of H13 powders (laser power is 225 W, scanning speed is 10 mm/s, and powder feed rate is 0.02 g/s). (*a*) t = 0.8 s (the first layer deposition proceeding); (*b*) t = 2.0 s (the first layer finished); (c) t = 2.8 s (the second layer deposition proceeding); (*d*) t = 4.0 s (the second layer deposition finished); (*e*) t = 5.0 s (the third layer deposition proceeding); and (*f*) t = 6.0 s (the third layer deposition finished) (the temperature unit is Celcius degree).

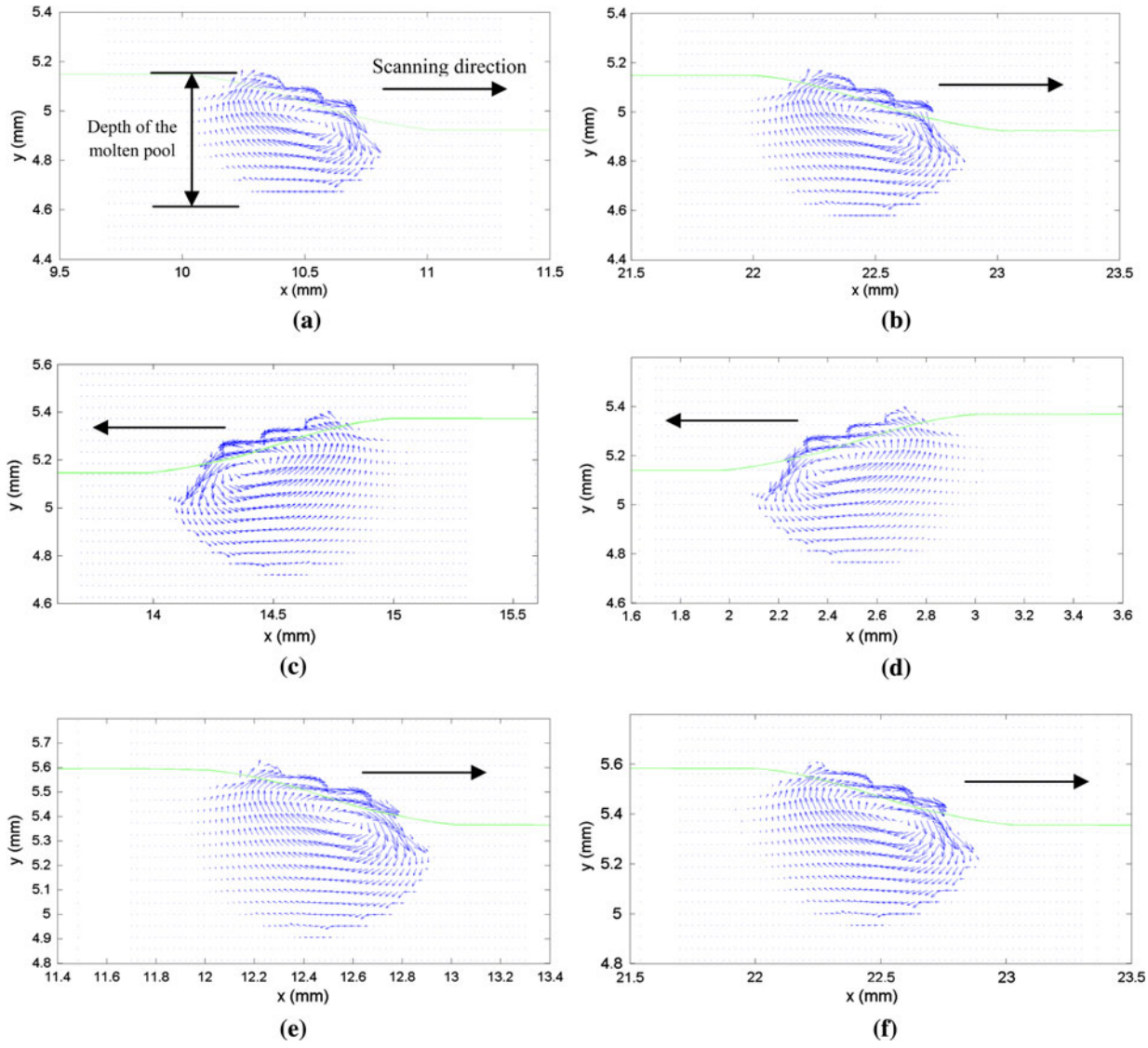

Fig. 5—Evolution of fluid flow in the molten pool during the laser multilayer cladding of H13 powder (laser power is 225 W, scanning speed is 10 mm/s, and powder feed rate is 0.02 g/s). (*a*) $t = 0.8$ s (the first layer deposition proceeding); (*b*) $t = 2.0$ s (the first layer finished); (c) $t = 2.8$ s (the second layer deposition proceeding); (*d*) $t = 4.0$ s (the second layer deposition finished); (*e*) $t = 5.0$ s (the third layer deposition proceeding); and (*f*) $t = 6.0$ s (the third layer deposition finished).

Because of the radiation of the laser beam with high energy density, the melted powder is deposited in the molten pool generated by the laser beam at the surface of the substrate. A higher temperature gradient exists in the molten pool of the deposited layer. A convection cycle exists in the molten pool because of the presence of a temperature-gradient surface tension, thermo-capillary force, and buoyancy. The evolution of the geometry and fluid flow of the liquid phase in the molten pool is shown in Figure 5. The temperature gradient, fluid flow, and profile of the molten pool reaches a steady state at about 1.034 seconds for the first layer deposition with 225 W of laser power, a 10-mm/s scanning speed, and a 0.02-g/s powder feed rate.

The evolution curve of the maximum temperature of the molten pool is shown in Figure 6. The temperature of the molten pool steadily increases when the laser beam advances along the deposition path. When the laser beam reaches the end of the clad bead, the signal is sent to the CNC positioning system to change the direction of motion and adjust the height of the laser deposition head to start the deposition with the second bead. During the activities, the laser beam is on, the feed of powder is on, and the substrate is stationary. These conditions result in an adaptive increase in the temperature of the molten pool and in an enlargement of the width and height of the deposited head. The laser power absorbed by the unit volume of the substrate during the change of direction of the motion can double in magnitude with respect to the laser power absorbed along the bead far from the corner. At the same time, the effect of laser power on the depth of the molten pool in the LMC process also is studied. Generally speaking, the depths of the molten pool tend to reach a steady state with an increase in the processing time, and those depths are larger with an increase in the laser power, as

shown in Figure 7. However, the depth of the molten pool becomes unsteady when the laser power is too low. For example, when the laser power is set at 150 W, the depth of the molten pool in the first layer deposition equals zero (Figure 7). This depth also is shown clearly in the temperature field simulation in Figure 6. When the laser power is set at 150 W, the lowest of three cases, the maximum temperature of the molten pool is reduced to no more than 1773 K (1500 °C), which is the melting point of the material. As the molten pool becomes weaker, the depth of the molten pool in the cladding process becomes unstable. The related experimental measurement also validates that the metallurgical bonding between the clad layer and the substrate possibly could fail, as shown in Figure 8.

The cross-sectional views of the clad under the continuous deposition process are shown in Figure 9. The relevant comparison of the clad height between the

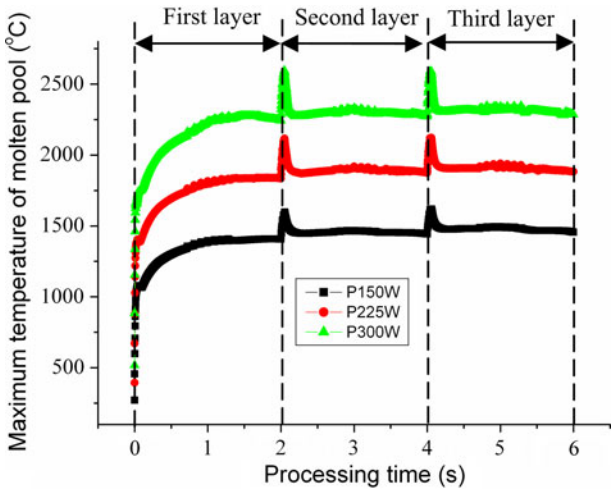

Fig. 6—Evolution curve of maximum temperature of the molten pool with processing time (laser power is 150, 225, and 300 W, scanning speed is 10 mm/s, and powder feed rate is 0.02 g/s).

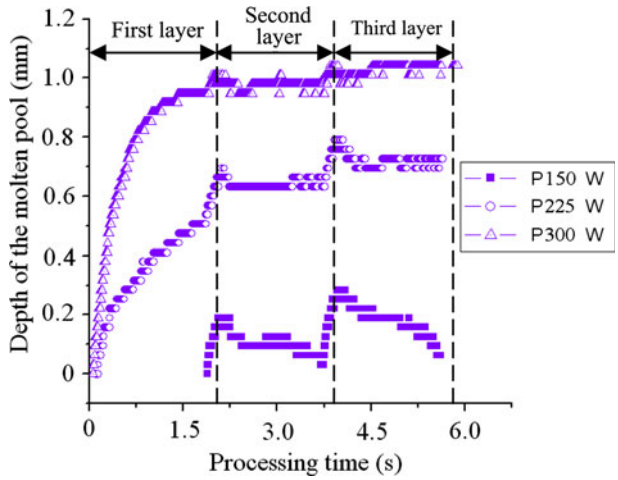

Fig. 7—Evolution curve of depth of the molten pool with processing time (laser power is 150, 225, and 300 W, scanning speed is 10 mm/s, and powder feed rate is 0.02 g/s).

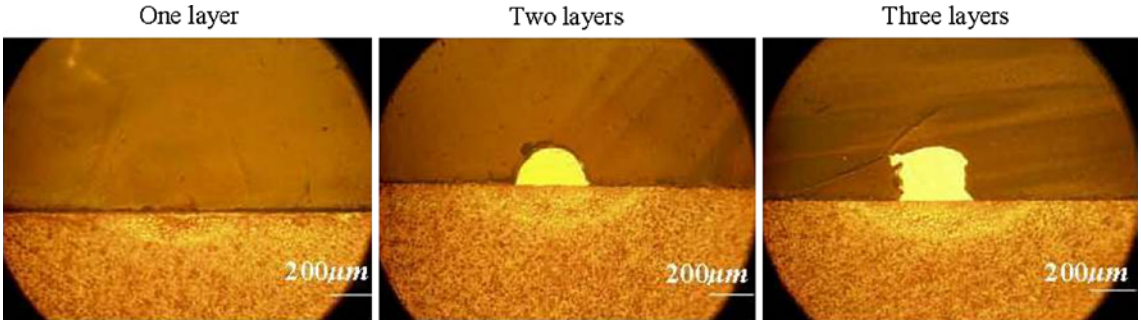

Fig. 8—Photos of cross-sectional views of the clad obtained by variable layers deposition at laser power of 150 W, scanning speed of 10 mm/s, and powder feed rate of S60 (~0.02 g/s).

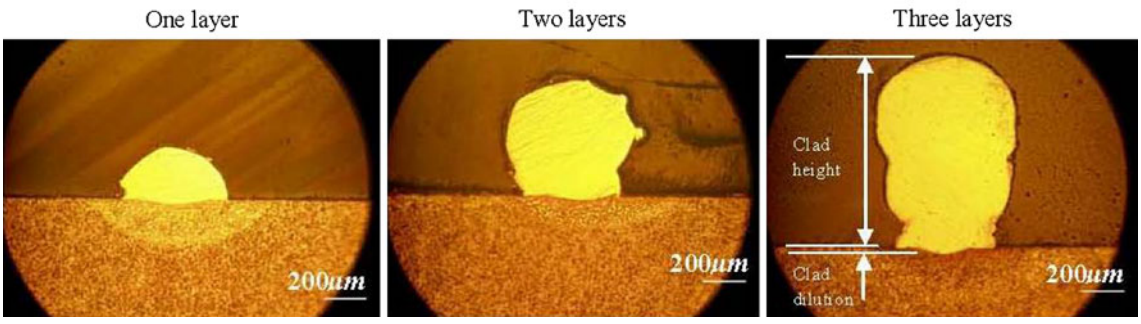

Fig. 9—Photos of cross-sectional views of the clad obtained by variable layers deposition at laser power of 300 W, scanning speed of 10 mm/s, and powder feed rate of S60 (~0.02 g/s).

simulation and experimental measurement also is plotted in Figure 10. The figure clearly indicates that the proposed unified model in which the heat transfer and fluid flow phenomena are considered accurately can predict the geometry of the clad in the laser cladding process. The errors shown in Figure 10 possibly lie with the assumption that the efficiency of powder usage is fixed in the multilayered cladding; however, the efficiency of powder usage is variable and increases a little bit with the increase of the deposition layer according to the previous experimental measurements.[27]

The related experimental results also show that the laser power obviously influences the geometry of the clad. Figure 11 shows the comparison of experimental and simulation results of the geometry of the three-layer clad obtained by different laser powers at a scanning speed of 10 mm/s and a powder feed rate of S60 (~0.02 g/s). Generally speaking, both the dilution and the height of the clad increase with an increase in the laser power. For laser power at 150 W, no dilution is observed of the bead into the substrate, and the metallurgical bond between the clad and substrate is the lowest of all three cases. When the laser power is 300 W, the dilution of the clad into the substrate is the largest of the three cases. In this case, the influence of the laser power on the efficient use of powder is ignored and kept as constant. But according to the related experimental investigation reported in Reference 27, the efficiency of powder usage is a function of the laser power. Generally, it increases with an increase in laser power.

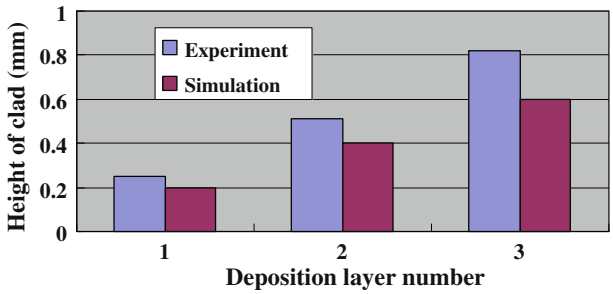

Fig. 10—Comparison of clad height obtained by numerical prediction and experimental measurement at laser power of 300 W, scanning speed of 10 mm/s and powder feed rate of S60 (~0.02 g/s).

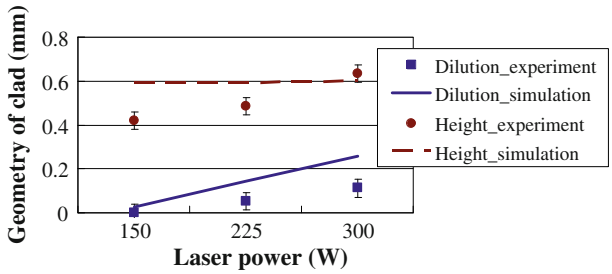

Fig. 11—Comparison of experimental and simulation results on the geometry of laser multilayered cladding as a function of laser power at a scanning speed of 10 mm/s and powder feed rate of S60 (~0.02 g/s).

The influence of the scanning speed on the geometry of the clad also is studied based on the experiment and numerical simulation. Figure 12 shows the related experimental and numerical results of the geometry sizes of the three-layer clad obtained under different scanning speeds at a laser power of 225 W and powder feed rate of S60 (~0.02 g/s). In general, the scanning speed has almost no obvious influence on the dilution and width of the clad for the fixed laser power and powder feed rate. However, the height of the clad reduces with an increase in the scanning speed. The related numerical results have a qualitative agreement with the experimental measurement.

The geometry of the clad is a function of the powder feed rate at a constant laser power and scanning speed in the laser multilayered cladding of H13 steel. With the increase in the powder feed rate, the height of the clad increases, and the dilution of the clad reduces. Figure 13 shows a comparison of the experimental and simulation results of the geometry of the three-layer clad as a function of the powder feed rate at a scanning speed of 10 mm/s and laser power of 225 W. A qualitative agreement exists between the numerical and experimental investigation. Although several assumptions are made to simplify the numerical model, a good agreement still is acquired between the solid–liquid–gas-unified model developed in this study and the experimental investigation.

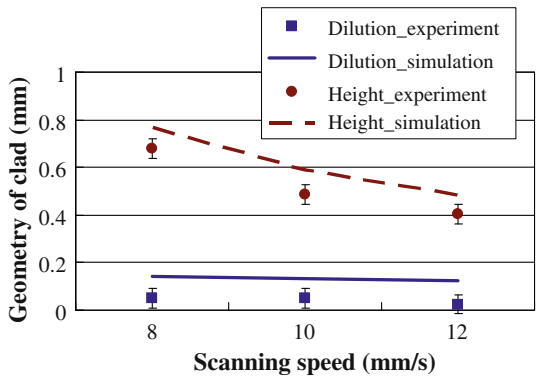

Fig. 12—Comparison of experimental and simulation results of the geometry of laser multilayered cladding as a function of the scanning speed at a laser power of 225 W and powder feed rate of S60 (~0.02 g/s).

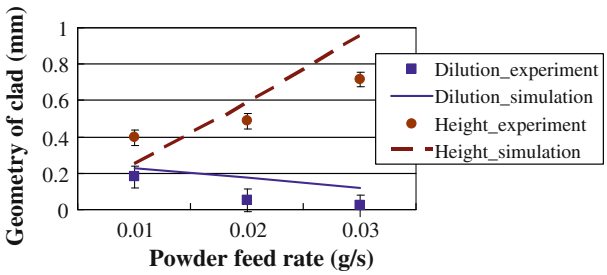

Fig. 13—Comparison of experimental and simulation results on the geometry of laser multilayered cladding as a function of powder feed rate at a laser power of 225 W and scanning speed of 10 mm/s.

V. CONCLUSIONS

A transient multiphase unified mathematical model with experimental validation is developed to investigate the temperature field and flow velocity field of the liquid phase in the laser-based multilayered cladding of H13 powder onto a substrate of AISI 4140 steel. A convection cycle exists in the molten pool during the laser-based multilayered cladding process resulting from the buoyancy force and temperature-gradient-induced surface tension. The effects of the laser power, scanning speed, and powder feed rate on the geometry of the clad are studied. The numerical results show that the exceedingly low power of the laser prevents the metallurgical bonding between the deposited layer and the substrate or the previous layer. However, the oversized power of the laser beam increases the depth of the molten pool and causes the deposited layer to collapse and to reduce further the surface quality of the clad. The relevant experiments also are performed to validate the numerical model, and a reasonable match exists between both sides. This model also can predict the whole heat-and-mass transfer process of other laser-based material processing technologies.

ACKNOWLEDGMENTS

The authors are grateful to Dr. Dechao Lin and Dr. Ehsan Foroozmehr, a research engineer and a former Ph.D. student, respectively, at the Research Center for Advanced Manufacturing for their valuable contribution in the experimental procedure design. The authors gratefully acknowledge support of this work by Grant No. EEC-0541952 from the National Science Foundation.

REFERENCES

1. C. Tassin, F. Laroudie, M. Pons, and L. Lelait: *Surface Coatings Technol.*, 1995, vols. 76–77, pp. 450–55.
2. H. Alemohammad, S. Esmaeili, and E. Toyserkani: *Mater. Sci. Eng. A*, 2007, vol. 456A, pp. 156–61.
3. W.H. Jiang and R. Kovacevic: *J. Mater. Process. Technol.*, 2007, vol. 186, pp. 331–38.
4. W.M. Steen: *Laser Material Processing*, Springer-Verlag, London, UK, 1991.
5. K. Partes and G. Sepold: *J. Mater. Process. Technol.*, 2008, vol. 195, pp. 27–33.
6. M. Qian, L.C. Lim, Z.D. Chen, and W.L. Chen: *J. Mater. Process. Technol.*, 1997, vol. 63, pp. 590–93.
7. H.K.D.H. Bhadeshia: *Mater. Sci. Technol.*, 2008, vol. 24, pp. 128–36.
8. H.-K. Lee: *J. Mater. Process. Technol.*, 2008, vol. 202, pp. 321–27.
9. J. Choi, L. Han, and Y. Hua: *ASME J. Heat Tran.*, 2005, vol. 127, pp. 978–86.
10. D. Salehi and M. Brandt: *Int. J. Adv. Manuf. Technol.*, 2006, vol. 29, pp. 273–78.
11. A. Kar and J. Mazumder: *J. Appl. Phys.*, 1987, vol. 61, pp. 2645–55.
12. A.F.A. Hoadley and M. Rappaz: *Metall. Trans. B*, 1992, vol. 23B, pp. 631–42.
13. L. Han, F.W. Liou, and K.M. Phatak: *Metall. Mater. Trans. B*, 2004, vol. 35B, pp. 1139–50.
14. E. Toyserkani, A. Khajepour, and S. Corbin: *Optic. Laser. Eng.*, 2004, vol. 41, pp. 849–67.
15. U. Duitsch, S. Schreck, and M. Rohde: *Int. J. Thermophys.*, 2003, vol. 24, pp. 731–40.
16. R. Komanduri and Z.B. Hou: *Int. J. Heat Mass Trans.*, 2001, vol. 44, pp. 2845–62.
17. S. Ghosh and J. Choi: *ASME J. Manuf. Sci. Eng.*, 2007, vol. 129, pp. 319–32.
18. D. Hu and R. Kovacevic: *Proc. IME B. J. Eng. Manuf.*, 2003, vol. 217, pp. 441–52.
19. X. He and J. Mazumder: *J. Appl. Phys.*, 2007, vol. 101, pp. 053113-1-9.
20. X. He, G. Yu, and J. Mazumder: *J. Phys. D Appl. Phys.*, 2010, vol. 43, pp. 015502-1-9.
21. R. Jendrzejewski, I. Kreja, and G. Śliwiński: *Mater. Sci. Eng. A*, 2004, vol. 379, pp. 313–20.
22. H. Zhang, F. Kong, G. Wang, and L. Zeng: *J. Appl. Phys.*, 2006, vol. 100, pp. 123522-1-9.
23. S. Chen, B. Merriman, S. Osher, and P. Smereka: *J. Comput. Phys.*, 1997, vol. 135, pp. 8–29.
24. W.D. Bennon and F.P. Incropera: *ASME J. Heat Tran.*, 1989, vol. 111, pp. 706–12.
25. W.D. Bennon and F.P. Incropera: *Numer. Heat Tran.*, 1988, vol. 13, pp. 277–96.
26. S.V. Patankar: *Heat Transfer and Fluid Flow*, Hemisphere Press, New York, NY, 1980.
27. Y.-L. Huang, G.-Y. Liang, J.-Y. Su, and J.-G. Li: *Model. Simulat. Mater. Sci. Eng.*, 2005, vol. 13, pp. 47–56.